



Fundamental Science of Energy 008

**"Development of a Thermoacoustic Model for
Evaluating Passive Damping Strategies"**

Syed Rehman and Jeff D. Eldredge

November 2005

This paper is part of the University of California Energy Institute's (UCEI) Energy Policy and Economics Working Paper Series. UCEI is a multi-campus research unit of the University of California located on the Berkeley campus.

UC Energy Institute
2547 Channing Way, # 5180
Berkeley, California 94720-5180
www.ucei.berkeley.edu

This report was issued in order to disseminate results of and information about energy research at the University of California campuses. Any conclusions or opinions expressed are those of the authors and not necessarily those of the Regents of the University of California, the University of California Energy Institute or the sponsors of the research. Readers with further interest in or questions about the subject matter of the report are encouraged to contact the authors directly.



Development of a Thermoacoustic Model for
Evaluating Passive Damping Strategies

Syed Rehman and Jeff D. Eldredge
Email: eldredge@seas.ucla.edu
Mechanical & Aerospace Engineering Department
University of California, Los Angeles

7 November 2005

Abstract

Lean premixed prevaporized (LPP) gas turbine generators have become popular in energy conversion applications to meet strict emission requirements. Because the combustion process is very lean, combustion instabilities due to acoustic perturbations are more likely to occur than in a less lean fuel combustion process. Current design of damping strategies for mitigating these instabilities is often based on empirical trial and error, which precludes the possibility of determining an optimal configuration. A combustion system whose elements consist of flames, passive dampers, and ducts must be optimized to reduce or completely eliminate combustion instabilities. Hence, a modular simulation tool is developed to examine the interaction of plane acoustic waves with typical combustion system elements. The simulation tool represents these interactions in the form of transfer matrices, which can be modularly arranged for exploring a variety of configurations. In this work, a heuristic gain-delay flame model is represented as a transfer matrix, which can be used to test damping devices. Similarly, transfer matrices representing a Helmholtz resonator and a perforated liner with bias flow are developed, and preliminary results are obtained.

1 Introduction

Thermoacoustic oscillations occur in a variety of applications such as rocket motors [4], jet engines [9, 16], and gas turbine generators [13, 15]. In this work a modular simulation tool is developed to examine the interaction of plane acoustic waves inside a duct with various sinks and/ or sources of sound. A previous planar flame model [6] is modified to exhibit the Rayleigh criterion [12], which results into a unstable acoustic system. A model for a Helmholtz resonator [5] and a perforated liner with bias flow [8] is also incorporated into the simulation tool for possible passive damping solutions.

Acoustic instabilities are a major concern in operating fuel-lean gas turbine generators and depending on the combustion system configuration, thermoacoustic oscillations may lead to instabilities. A lean premixed prevaporized (LPP) combustion process runs at a lower temperature lowering pollutant emissions such as NO_x and CO . The production of NO_x and CO chemically is an endothermic process; due to the energy consumption nature of these processes, such a reaction is more probable at higher temperatures. An LPP process lowers the adiabatic flame temperature and hence lowers the overall temperature inside the combustion chamber, significantly reducing the production of undesirable emissions.

One problematic outcome of running a LPP combustion process is that the system is more prone to combustion instabilities [3, 14]. The LPP combustion process is characterized by a greater sensitivity to fluctuations in the equivalence ratio ϕ [12]. Flame heat release in gas turbine combustion chambers is generally unsteady. The unsteady heat release causes fluctuations in the local density, pressure and velocity which propagate away from the flame in the form of acoustic waves [7, 2]. These oscillations reflect off the chamber boundaries (compressor, turbine, etc) and propagate back towards the flame resulting in deviations in the fuel and air mixture and possibly amplifying the unsteady behavior of the heat release [14, 12]. If this interaction is in phase (i.e the Rayleigh Criterion is satisfied) this process becomes self-excited and may lead the system to experience large amplitude oscillations, potentially causing structural damage.

In the early rockets, acoustic instabilities were also a major problem which eventually were overcome with extensive research on passive control. Control strategies typically consist of inclusion of baffles and/or geometric modifications [14]. Furthermore, unlike rocket motors, combustion instabilities in LPP gas turbine generators are excited by multiple means, such as rotating machinery, fuel mixing, and multiple flame mechanisms. A simple approach, for example geometric modifications, may not be sufficient to completely stabilize the system. Therefore, a more robust mechanism is needed to overcome these instabilities. One effective solution is the utilization of passive acoustic damping devices which remove energy from the acoustic field and thereby weaken the feedback cycle. One conventional damper is the Helmholtz resonator, which is a cavity with a neck connected to the system through a small orifice. Near its resonance frequency, the resonator experiences large amplitudes of acoustic oscillation in its neck. The high amplitude oscillations in the neck dissipate acoustic energy by means of vortex shedding at the neck-duct interface and viscous effects of fluid and wall interaction [1].

A Helmholtz resonator, however, is only effective in the limited bandwidth near resonance. Also, the resonant oscillation in the neck is heavily dependent on the external pressure fluctuations, so the resonator fails to dissipate acoustic energy if placed near a pressure node. A damping system that may overcome some of these limitations is a perforated liner with bias flow, which has an array of orifices across the length and circumference of its cylindrical shell. Harmonic pressure differences across the aperture excite periodic vortex shedding, and shed vortices are convected away by the bias flow [11]. This process converts the acoustic energy into mechanical energy, which eventually is dissipated into heat [8]. A liner, unlike a localized resonator, is spread over a length, consequently it is effective over a relatively larger range of frequencies and locations.

The focus of this work is to investigate the effectiveness of a perforated liner with bias flow as a damping mechanism for thermoacoustic instabilities in gas turbine combustion chambers. A particular goal of this research is to explore the robustness of damping to changes in liner geometry and combustor conditions, and contrast it with results achieved with a Helmholtz resonator. Another interest is to develop a generic modular acoustic simulation tool to numerically investigate multiple system configurations with relative ease, to facilitate damper design strategies beyond empirical trial and error approaches. This work relies on numerical modeling of the damping devices in a simple ducted flame geometry. Thus, conclusions drawn are meant to provide guidance for future experimental studies.

The modular simulation tool, discussed in § 2, is based on plane wave theory and relates these propagating waves in and out of an acoustic source and/or sink with the use of transfer functions. A heuristic flame model, discussed in § 3.1.1, is similar to the one in [6] with an adjustment of a gain-delay modification [12] imposed to satisfy the Rayleigh Criterion. The model for the perforated liner model, discussed in § 3.2.2, is adapted from [8], in which its accuracy was verified experimentally. The perforated liner model will be numerically compared with a model for a Helmholtz resonator [5], which also has been verified experimentally and is discussed in § 3.2.1.

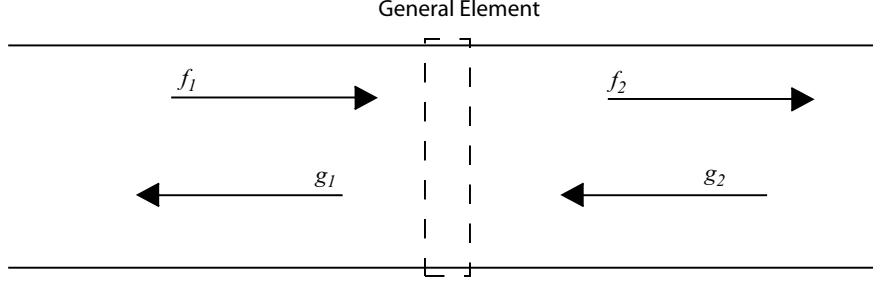


Figure 1: A duct with a general element.

2 Methodology

Acoustic perturbations in a duct consist of pressure, velocity and density perturbations. Because characteristic frequencies in the system of interest are below cut-on of higher order modes, we are modeling behavior with plane acoustic waves, which satisfy a linear one dimensional wave equation. For a single frequency, a solution is given by

$$p'(x, t) = \exp(i\omega t) \left[f \exp\left(\frac{-i\omega x}{\bar{c} + \bar{u}}\right) + g \exp\left(\frac{i\omega x}{\bar{c} - \bar{u}}\right) \right] \quad (1)$$

where f and g are wave amplitudes propagating downstream and upstream in the duct respectively. ω , \bar{c} and \bar{u} is the frequency, the mean speed of sound and the mean velocity inside the duct. From the definition of the speed of sound $c^2 = dp/d\rho|_s$ and the linear relationship between pressure and density $p' = \rho' dp/d\rho$ the density perturbation can be expressed as

$$\rho' = p'/c^2 \quad (2)$$

Furthermore, using equations (1) and (2) the velocity perturbations can be expressed as follows

$$u' = \pm \frac{p'}{\bar{\rho}\bar{c}} \quad (3)$$

where $\bar{\rho}$ is the mean density. The positive sign is chosen for a forward propagating wave and negative for a backward propagating wave.

For an arbitrary element in a system (e.g. flame, dampers, etc.), as depicted in figure 1, the pressure and velocity jump conditions can be represented in the matrix form as follows.

$$\begin{bmatrix} f_2 \\ g_2 \end{bmatrix} = Y^{-1}X \begin{bmatrix} f_1 \\ g_1 \end{bmatrix} \quad (4)$$

For a duct with only one element applying the upstream and the downstream boundary conditions

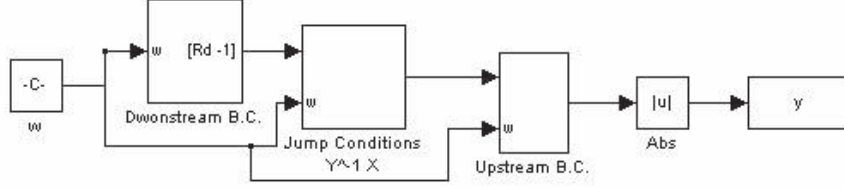


Figure 2: Simulink approach to acoustics.

with the transfer matrix gives the following matrix equation

$$\begin{bmatrix} R_d & -1 \end{bmatrix} Y^{-1} X \begin{bmatrix} R_u \\ 1 \end{bmatrix} = 0 \quad (5)$$

where R_u and R_d are upstream and downstream reflection coefficients respectively. Note, due to the homogeneous nature of this equation set, the wave amplitudes cannot be solved for. The only non-trivial solutions possible are the frequencies of the system. These frequencies are generally complex, and the imaginary part corresponds to exponential growth or decay (negative values give growth). If the system consisted of n elements, there will be $n (2) \times (2)$ transfer matrices representing each element in the system.

$$\begin{bmatrix} R_d & -1 \end{bmatrix} (Y^{-1} X)_n \dots (Y^{-1} X)_1 \begin{bmatrix} R_u \\ 1 \end{bmatrix} = 0 \quad (6)$$

One advantage of transfer matrices is that they can be easily modeled in a block diagram approach, connecting elements in a modular fashion. This approach allows the use of graphical software such as Simulink to perform the analysis and virtually no coding is required. Figure 2 shows a Simulink model for duct acoustics of one element in a simple straight duct.

In a system with entropy generation, the acoustic and entropy wave interaction modifies this approach slightly. As discussed in § 3.1.1 whenever there is heat addition entropy is generated. An entropy wave propagating downstream of the flame can always be related to the upstream density and temperature perturbations. This interaction can be incorporated into the transfer matrix approach.

$$\begin{bmatrix} f_2 \\ g_2 \\ S \end{bmatrix} = Y^{-1} X \begin{bmatrix} f_1 \\ g_1 \end{bmatrix} + Y^{-1} C \hat{Q}$$

note, Y is of dimension 3×3 , X is of dimension 3×2 and C is of dimension 3×1 . \hat{Q} represents heat addition fluctuations. Because the goal here is to solve for the frequency of acoustic oscillations, and not the entropy wave itself, the last row in the transfer matrix, which represents the entropy wave, can be ignored.

Applying the boundary conditions to the first two rows of the transfer matrix provides the following homogeneous equation

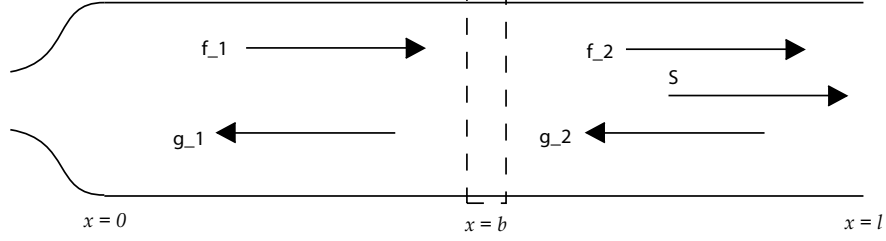


Figure 3: Flame duct system

$$\begin{bmatrix} R_1^d & R_2^d \end{bmatrix} (A + B) \begin{bmatrix} R_2^u \\ -R_1^u \end{bmatrix} = 0$$

where A and B are the first two rows of $Y^{-1}X$ and $Y^{-1}C$ respectively, and the $R_{1,2}^{u,d}$ represent the upstream and downstream reflection coefficients.

All the elements upstream of the flame can be represented with 2×2 matrices while all the elements downstream of the flame are represented with 3×3 matrices. However, the transfer matrix due to the flame (or, in general, due to an element that generates entropy) is a 3×2 matrix, which leads to dimensional consistency throughout the matrix multiplication for all the elements.

3 Model

3.1 Heuristic Flame Acoustics

3.1.1 Adapted Flame Model

The flame model utilized in this work is adapted from Dowling [6]. The following derivation uses a similar approach as used in Dowling [6], to acquire a transfer matrix governing velocity and pressure jump conditions across the flame.

The acoustic perturbations upstream, denoted by subscript 1, of the flame zone are given by

$$\begin{aligned} p'(x, t) &= \exp(i\omega t) \left[f_1 \exp\left(\frac{-i\omega x}{\bar{c}_1(1 + \bar{M}_u)}\right) + g_1 \exp\left(\frac{i\omega x}{\bar{c}_1(1 - \bar{M}_u)}\right) \right] \\ u'(x, t) &= \frac{\exp(i\omega t)}{\bar{\rho}_1 \bar{c}_1} \left[f_1 \exp\left(\frac{-i\omega x}{\bar{c}_1(1 + \bar{M}_u)}\right) - g_1 \exp\left(\frac{i\omega x}{\bar{c}_1(1 - \bar{M}_u)}\right) \right] \\ \rho'(x, t) &= p'(x, t) / \bar{c}_1^2 \\ c_p T'(x, t) &= p'(x, t) / \bar{\rho}_1 \end{aligned}$$

where f and g are wave amplitudes and \bar{M}, \bar{c} and $\bar{\rho}$ are the mean quantities of the Mach number, speed of sound and density respectively. Downstream of the flame zone, denoted by subscript 2,

the perturbations are given by

$$\begin{aligned}
p'(x, t) &= \exp(i\omega t) \left[f_2 \exp\left(\frac{-i\omega x}{\bar{c}_2(1+\bar{M}_d)}\right) + g_2 \exp\left(\frac{i\omega x}{\bar{c}_2(1-\bar{M}_d)}\right) \right] \\
u'(x, t) &= \frac{\exp(i\omega t)}{\bar{\rho}_2 \bar{c}_2} \left[f_2 \exp\left(\frac{-i\omega x}{\bar{c}_2(1+\bar{M}_d)}\right) - g_2 \exp\left(\frac{i\omega x}{\bar{c}_2(1-\bar{M}_d)}\right) \right] \\
\rho'(x, t) &= p'(x, t) / \bar{c}_2^2 - \frac{S \bar{\rho}_2}{c_p} \exp(i\omega(t - x/\bar{u}_2)) \\
c_p T'(x, t) &= p'(x, t) / \bar{\rho}_2 - \frac{S \bar{c}_2^2}{(\gamma - 1) c_p} \exp(i\omega(t - x/\bar{u}_2))
\end{aligned}$$

where S is the amplitude of the entropy wave and γ is the ratio of specific heats. and substitution of the harmonic form of these perturbations into mass, momentum and energy conservation across the flame gives the following transfer matrices

$$Y \begin{bmatrix} f_2 \\ g_2 \\ S \end{bmatrix} = X \begin{bmatrix} f_1 \\ g_1 \end{bmatrix} + C \hat{Q} \quad (7)$$

where, Y is

$$Y = \begin{bmatrix} (1+M_2)e_1 & -(1-M_2)e_2 & M_2^2 \\ \frac{\bar{c}_2}{\bar{c}_1}(1-M_2^2)e_3 & \frac{\bar{c}_2}{\bar{c}_1}(1-M_2^2)e_4 & -\frac{\bar{c}_2}{\bar{c}_1}M_2^2 \\ (1+M_2)a_3e_3\frac{\bar{c}_2}{\bar{c}_1} & (1-M_2)a_4e_4\frac{\bar{c}_2}{\bar{c}_1} & -\frac{\bar{c}_2}{\bar{c}_1}\frac{1}{2}M_2^2 \end{bmatrix} \quad (8)$$

and X is

$$X = \begin{bmatrix} \frac{\bar{c}_2}{\bar{c}_1}(1+M_1)e_1 & -\frac{\bar{c}_2}{\bar{c}_1}(1-M_1)e_2 \\ (1+M_1)^2e_1 & (1-M_1)^2e_2 \\ (1+M_1)a_1e_1 & (1-M_1)a_2e_2 \end{bmatrix} \quad (9)$$

and C is

$$C = \begin{bmatrix} 0 \\ 0 \\ 1 \end{bmatrix} \quad (10)$$

where

$$\begin{aligned}
e_1 &= \exp(-i\omega b/\bar{c}_1(1+\bar{M}_1)), \quad e_2 = \exp(i\omega b/\bar{c}_1(1-\bar{M}_1)) \\
e_3 &= \exp(-i\omega b/\bar{c}_2(1+\bar{M}_2)), \quad e_4 = \exp(i\omega b/\bar{c}_2(1-\bar{M}_2))
\end{aligned}$$

and

$$\begin{aligned}
a_1 &= M_1 + \frac{1}{2}M_1^2 + (\gamma - 1)^{-1}, \quad a_2 = M_1 - \frac{1}{2}M_1^2 - (\gamma - 1)^{-1} \\
a_3 &= M_2 + \frac{1}{2}M_2^2 + (\gamma - 1)^{-1}, \quad a_4 = M_2 - \frac{1}{2}M_2^2 - (\gamma - 1)^{-1}
\end{aligned}$$

3.1.2 Unsteady Heat Release

An expression for the unsteady heat release can be derived by energy balance across the flame.

$$Q = \dot{m}_f \Delta h_{rxn} = (\dot{m}_o + \dot{m}_f) \Delta h_{0,12} \quad (11)$$

note, subscripts o, f and 0 represent oxidizer, fuel and stagnation condition. Also, the heat of reaction Δh_{rxn} is not a function of time and space and is only dependent on the chemical properties of the fuel.

In this work only small fluctuations from mean conditions are considered (where $|Q'| \ll |\bar{Q}|$). So, the total heat release Q can be represented as $\bar{Q} + Q'$, a steady heat release term \bar{Q} and a unsteady heat release term Q' . Furthermore, due to linearity higher order terms can be neglected.

Linearizing equation (11) and assuming no unsteady heat input per unit mass or $\Delta h'_{0,12} \rightarrow 0$ leads to

$$\dot{m}'_f \Delta h_{rxn} = Q' = (\dot{m}'_o + \dot{m}'_f) \Delta \bar{h}_{0,12} \quad (12)$$

note, the mass flux of fuel can be related to the mass flux for the oxidizer by the actual fuel to oxidizer ratio $f^* = \dot{m}_f / \dot{m}_o$ and if $f \ll 1$, which is true for lean fuel condition, then the heat release expression utilized by Dowling is acquired

$$Q' = (\dot{m}'_o) \Delta \bar{h}_{0,12}$$

relating \dot{m}'_o to the local acoustic waves gives

$$\hat{Q} = \Delta \bar{h}_{0,12} \begin{bmatrix} (1 + M_1)e_1/c_1^2 & -(1 - M_1)e_2/c_1^2 \end{bmatrix} \begin{bmatrix} f_1 \\ g_1 \end{bmatrix} \quad (13)$$

3.1.3 Time Delay

In order to explore the effect of damping on an unstable combustion system, the model presented in equation (13) must be extended to allow instability. According to the Rayleigh criterion, a combustion system experiences acoustic instabilities when the pressure and unsteady heat release fluctuations are in phase or the unsteady heat release is driving the pressure fluctuations and vice versa. One option is to incorporate time delays, which physically exist in combustion systems (for example, the convection time for the fuel from the injector to the flame), into the unsteady heat release satisfying the Rayleigh criterion. With the addition of an arbitrary time delay τ_d equation (13) becomes

$$Q'(t, x) = \dot{m}'(t - \tau_d, x) c_p (\bar{T}_{02} - \bar{T}_{01}) \quad (14)$$

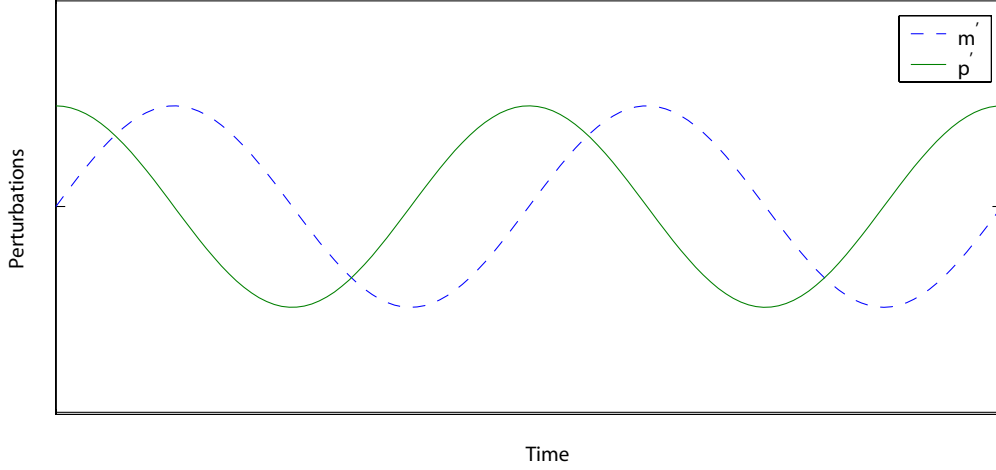


Figure 4: Schematic depicts the phase relation between pressure, mass flow, and heat release oscillations of the current heat release model.

substituting $m'(t, x) = \bar{\rho}_1 u'_1(t, x) + \rho'_1(t, x) \bar{u}_1$ into equation (14) gives

$$Q'(t, x) = (\bar{\rho}_1 u'_1(t - \tau_d, x) + \rho'_1(t - \tau_d, x) \bar{u}_1) cp (\bar{T}_{02} - \bar{T}_{01}) \quad (15)$$

The unsteady heat addition with a time delay changes Q' discussed in § 3.1.2 to

$$Q' = \Delta \bar{h}_{0,12} \exp[-i\omega\tau_d] \begin{bmatrix} (1 + M_1)e_1/c_1^2 & -(1 - M_1)e_2/c_1^2 \end{bmatrix} \begin{bmatrix} f_1 \\ g_1 \end{bmatrix}$$

The two major contributors of unsteady heat release are the acoustic fluctuations at the fuel injector and at the base of the flame [12]. The injectors are usually located upstream of the flame, hence the fluctuations at the injector convect to the flame after some time, τ_{conv} .

The fluctuation at the base of the flame disturb the heat release since the fuel is burned unevenly in accordance with the shape of the flame. The shape of the flame determines the time, τ_{eq} , required to consume the fuel completely [12]. For a planar flame, the complete consumption of the fuel is even, or $\tau_{eq} = 0$.

The convection time, τ_{conv} , is the distance the perturbations must travel divided by the mean velocity at which these perturbations travel downstream. That is,

$$\tau_{conv} = \|l_{inj}\|/\bar{u}$$

The current model given by equation (12) assumes that the unsteady heat release is in phase with the flow perturbation. For a choked inlet or a mass flow perturbation node at the inlet, the

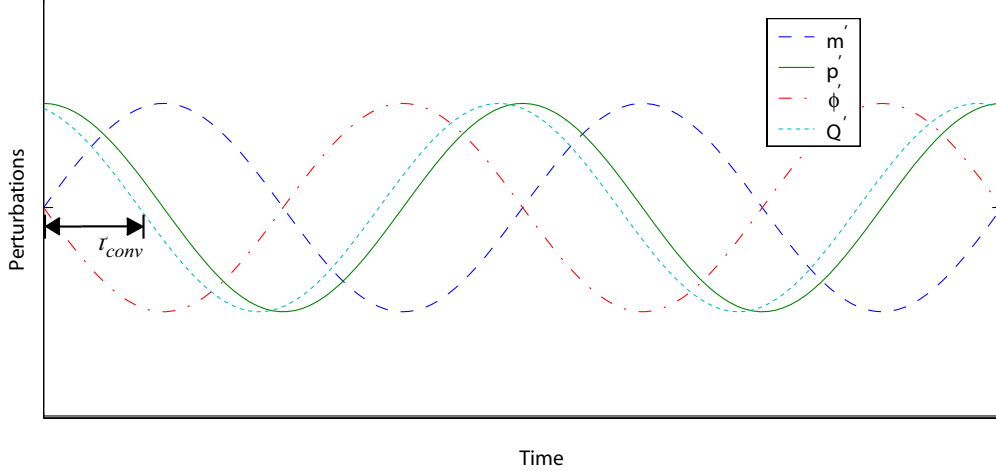


Figure 5: Schematic depicts the phase relation between pressure, mass flow, equivalence ratio, and heat release oscillations of the modified heat release model with time delays.

pressure perturbation leads the mass flow perturbation by 90 degrees, hence the Rayleigh criterion is not satisfied. Please refer to figure 4 for a graphical representation.

In general, the heat release is not in phase with the fluctuations in the equivalence ratio, ϕ' . The heat release for a planar flame lags ϕ' by the convective time delay τ_{conv} . Also, unlike the previous assumption ϕ' is not in phase with oscillation in the mass flow, \dot{m}'_o , for a choked fuel injector configuration. The oscillation in ϕ is given by,

$$\frac{\phi'}{\bar{\phi}} = \frac{\dot{m}'_f/\bar{\dot{m}}_f - \dot{m}'_o/\bar{\dot{m}}_o}{1 + \dot{m}'_o/\bar{\dot{m}}_o}$$

so for a choked injector $\dot{m}'_f \rightarrow 0$, indicating that the oscillation in ϕ lags \dot{m}'_o by 180 degrees.

Hence, the phase of the unsteady heat release Q' lags the phase of \dot{m}'_o by a time delay of τ_d where

$$\tau_d = \tau_{conv} + \pi/\omega$$

Referring to figure 5, to satisfy Rayleigh's criteria the convective time delay τ_{conv} for a choked inlet & choked injector is given by [12]

$$\frac{\tau_{conv}}{T} = C_n = n - 3/4 \quad \text{where } n = 1, 2, 3 \dots \quad (16)$$

C_n centers around a region over which instability occurs. The limits of the region are ± 90 degrees phase difference between pressure and heat release oscillations. Or, the unstable region is given by (Lieuwen),

$$C_n - 1/4 < \tau_{conv}/T < C_n + 1/4 \quad (17)$$

3.1.4 Mach Number Downstream of the Flame

Applying momentum conservation across the flame

$$p_1 - p_2 = \rho_2 u_2^2 - \rho_1 u_1^2 \quad (18)$$

Assuming the specific heat ratio γ is constant across the flame and applying the definition of mach number, $M^2 = u^2 / \left(\frac{\gamma p}{\rho}\right)$ to equation (18) gives the following upstream and downstream pressure ratio relation to upstream and downstream mach numbers.

$$\frac{p_1}{p_2} = \frac{1 + \gamma M_2^2}{1 + \gamma M_1^2} \quad (19)$$

Now, by observing mass conservation across the control volume

$$\rho_1 u_1 = \rho_2 u_2 \quad (20)$$

and utilizing the ideal gas law $p = \rho RT$ and the stagnation temperature definition $\frac{T_0}{T} = 1 + \frac{\gamma-1}{2} M^2$, equation (20) becomes

$$\frac{p_1}{p_2} = \frac{M_2}{M_1} \sqrt{\frac{T_{01} \left(1 + \frac{\gamma-1}{2} M_2^2\right)}{T_{02} \left(1 + \frac{\gamma-1}{2} M_1^2\right)}} \quad (21)$$

combining equations (19) and (21) relates the stagnation temperature ratio across the flame to the upstream and downstream mach numbers [10]:

$$\frac{T_{02}}{T_{01}} = \frac{M_2^2 \left(1 + \frac{\gamma-1}{2} M_2^2\right) (1 + \gamma M_1^2)^2}{M_1^2 \left(1 + \frac{\gamma-1}{2} M_1^2\right) (1 + \gamma M_2^2)^2} \quad (22)$$

3.2 Damper Models

3.2.1 Duct/ Resonator System with a Mean Flow

A Helmholtz resonator, depicted in figure 6, can act as an extremely effective acoustic damper. Near its resonance, the resonator experiences large amplitudes of acoustic oscillation in its neck. The high amplitude oscillations in the neck dissipate acoustic energy by the means of vortex shedding at the neck duct interface and by the means of viscous effects of fluid and wall interaction.

A Helmholtz resonator is analogous to a capacitor. A capacitor stores electrical energy within its electrical field, likewise, a Helmholtz resonator holds acoustic energy within its volume. Hence, like an alternating current electrical circuit the resonator can easily be modeled utilizing the concept of acoustic impedance.

$$Z = p'/u'$$

The acoustic impedance is also analogous to the electrical impedance. The electrical impedance is the ratio of the voltage to the current, where the voltage is the driver and the current is the flow. Similarly, the acoustic impedance is the ratio of the pressure perturbation to the velocity perturbation, where the pressure perturbation is the driver and the velocity perturbation is the flow.

Utilizing the concept of acoustic impedance the resonator can essentially be modeled after a *RLC* series circuit. The viscous resistance and the vortex shedding is similar to a resistor. The volume of the resonator is similar to a capacitor. Last, the neck of the resonator is analogous to an inductor. The impedance for each component is given by

$$\begin{aligned} \text{Volume } Z_V &= i \frac{\rho c^2}{\omega V} \\ \text{Neck } Z_N &= -i \omega \rho \frac{l_n}{S_n} \\ \text{Vortex Shedding } Z_R &= \frac{i \omega \rho}{K_r} \end{aligned}$$

For simplicity, only the vortex shedding resistance is being taken into account. Here, V is the volume of the resonator. l_n and S_n are the length and the cross-sectional area of the neck respectively. And, K_a is the Rayleigh conductivity, which was derived by Howe [11] for an aperture with mean bias flow.

$$K_a = 2a (\gamma + i\delta) \tag{23}$$

Generally, γ and δ are complicated functions of Strouhal number. However, for low frequency perturbations these functions are approximated as:

$$\begin{aligned} \gamma &\approx 0 \\ \delta &\approx \frac{\pi a \omega}{4 \bar{u}_n} \end{aligned}$$

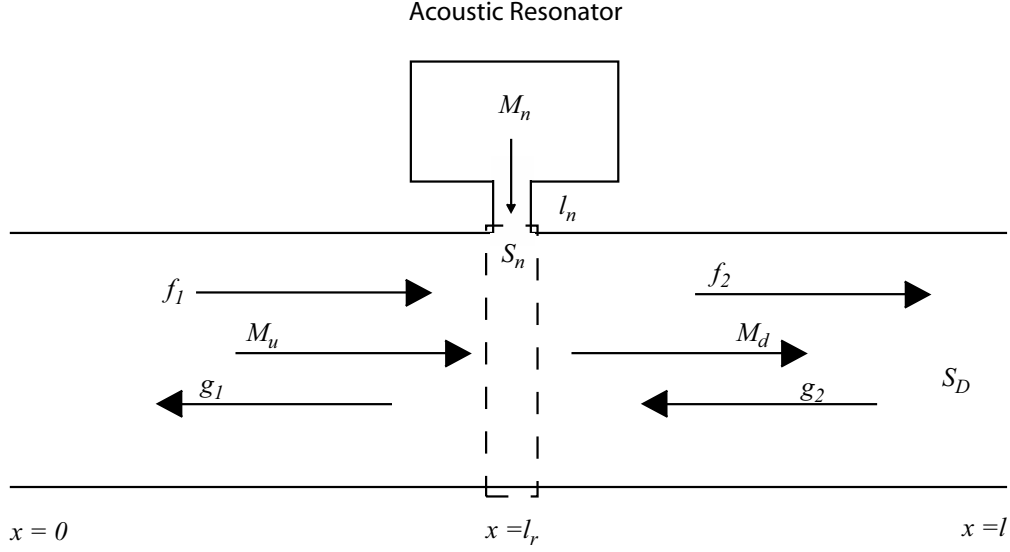


Figure 6: Ducted resonator system

The stagnation enthalpy perturbation across a resonator with a mean flow is continuous. This can be shown by conducting a mass, momentum and energy balance across the control volume, please see [5]. A mass and momentum balance across the resonator is utilized to formulate the transfer matrices for the system. For simplicity, the assumption of the mean flow being constant across the control volume is made. This is certainly not a bad assumption, since the mean mass flow through the neck is typically at least an order of magnitude less than the mean mass flow through the duct, $\dot{m}_n \ll \dot{m}$. Mass balance gives

$$\rho'_1 \bar{u}_1 + \bar{\rho}_2 u'_1 - (\rho'_2 \bar{u}_2 + \bar{\rho}_2 u'_2) = -\bar{\rho}_n c \frac{S_n}{S_D} \left(\frac{\rho'_n}{\bar{\rho}_n} M_n + \frac{u'_n}{\bar{u}_n} \right)$$

please note that the perturbations in density and velocity in the neck are the same order of magnitude and the bias flow Mach no. is typically significantly smaller than one, $M_n \ll 1$, hence the density perturbations in the neck are negligible to the neck velocity perturbations. Furthermore, the neck velocity perturbations can be related to the stagnation enthalpy perturbations upstream of the resonator which in turn can be related to the pressure oscillations and the Mach no. upstream of the control volume.

$$u'_n = \rho h'_{0,n} / S_n Z_n = p'_1 (1 \pm M) / S_n Z_n$$

The momentum balance across the control volume gives the pressure jump condition

$$p'_1 + \rho'_1 \bar{u}_1^2 + 2\bar{\rho}_1 \bar{u}_1 u'_1 = p'_2 + \rho'_2 \bar{u}_2^2 + 2\bar{\rho}_2 \bar{u}_2 u'_2$$

Substituting in the harmonic wave functions and non-dimensionalizing gives the following two transfer matrices

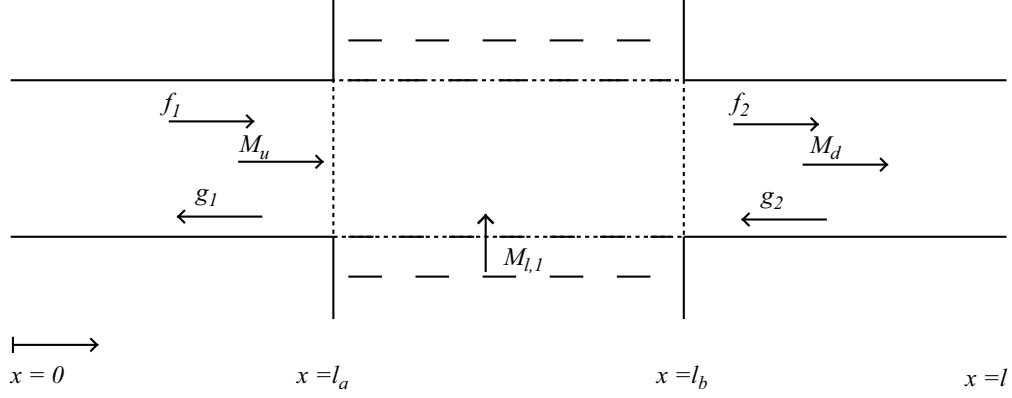


Figure 7: Perforated liner ducted system

$$\tilde{x}^R = \begin{bmatrix} (1+M)(1+Y)e_1 & (1-M)(1+Y)e_2 \\ (1+M)^2e_1 & (1-M)^2e_2 \end{bmatrix}$$

$$\tilde{y}^R = \begin{bmatrix} (1+M)e_1 & (1-M)e_2 \\ (1+M)^2e_1 & (1-M)^2e_2 \end{bmatrix}$$

where Y is the non-dimensional admittance of the resonator and is given by

$$Y = \frac{\rho c}{S_D Z_n} = \left\{ 2M_n \frac{S_D}{S_n} + i \left(\frac{l S_D}{V} \frac{1}{\tilde{\omega}} + \tilde{\omega} \frac{l_n}{l} \frac{S_D}{S_n} \right) \right\}^{-1}$$

and

$$e_1 = \exp(-i\tilde{\omega}l_r/l(1+M))$$

$$e_2 = \exp(i\tilde{\omega}l_r/l(1-M))$$

3.2.2 Perforated Liner with Bias Flow

A perforated liner ducted system consists of a circular duct of length l and a perforated liner of length $l_p = l_b - l_a$. The system is subject to an upstream axial flow u_u and a bias flow v_1 . Note, both flows are small and have the same stagnation temperature associated with them hence the mean speed of sound and density, \bar{c} and $\bar{\rho}$ respectively, are constant across the control volume. So, the downstream velocity is then given by $u_d = u_u + (C_1 l_p / S_p) v_1$ where C_1 and S_p is the circumference and the cross-sectional area for liner 1 respectively.

As before, please see § 2, this model is based on plane wave theory, i.e, f_1 and f_2 are amplitudes of waves traveling downstream along the duct while g_1 and g_2 are amplitudes of waves traveling

upstream. Substituting in the following non-dimensional variables into the harmonic stagnation enthalpy and velocity perturbation equations

$$\begin{aligned} x &\rightarrow x/l, \quad t \rightarrow \bar{c}t/l, \quad u \rightarrow u/\bar{c}, \quad v \rightarrow v/\bar{c} \\ B &\rightarrow B/\bar{c}, \quad \rho \rightarrow \rho/\bar{\rho}, \quad p \rightarrow p/(\bar{\rho}\bar{c}^2), \quad \omega \rightarrow \omega l/\bar{c} \end{aligned}$$

for $0 < x < l_a$ we get

$$\begin{aligned} B'(x, t) &= \exp(i\omega t) \left[f_1 \exp\left(\frac{-i\omega x}{1 + M_u}\right) + g_1 \exp\left(\frac{i\omega x}{1 - M_u}\right) \right] \\ u'(x, t) &= \exp(i\omega t) \left[f_1 \exp\left(\frac{-i\omega x}{1 + M_u}\right) - g_1 \exp\left(\frac{i\omega x}{1 - M_u}\right) \right] \end{aligned}$$

for $l_a < x < l_b$

$$\begin{aligned} B(x, t) &= \bar{B} + \hat{B}(x) \exp(i\omega t) \\ u(x, t) &= \bar{u}(x) + \hat{u}(x) \exp(i\omega t) \\ \bar{u}(x) &= M_u + \frac{C_1 l}{S_p} x \end{aligned}$$

and for $l_b < x < l$

$$\begin{aligned} B'(x, t) &= \exp(i\omega t) \left[f_2 \exp\left(\frac{-i\omega x}{1 + M_d}\right) + g_2 \exp\left(\frac{i\omega x}{1 - M_d}\right) \right] \\ u'(x, t) &= \exp(i\omega t) \left[f_2 \exp\left(\frac{-i\omega x}{1 + M_d}\right) - g_2 \exp\left(\frac{i\omega x}{1 - M_d}\right) \right] \end{aligned}$$

Note, the stagnation enthalpy and velocity perturbations are continuous across $x = l_a$ and $x = l_b$

$$\hat{B}(l_a) = f_1 e_1 + g_1 e_2 \tag{24}$$

$$\hat{u}(l_a) = \frac{f_1}{1 + M_u} e_1 + \frac{g_1}{1 - M_u} e_2 \tag{25}$$

$$\hat{B}(l_b) = f_2 e_3 + g_2 e_4 \tag{26}$$

$$\hat{u}(l_b) = \frac{f_2}{1 + M_d} e_3 + \frac{g_2}{1 - M_d} e_4 \tag{27}$$

where

$$\begin{aligned} e_1 &= \exp\left(\frac{-i\omega l_a}{1 + M_u}\right), \quad e_2 = \exp\left(\frac{i\omega l_a}{1 - M_u}\right) \\ e_3 &= \exp\left(\frac{-i\omega l_b}{1 + M_d}\right), \quad e_4 = \exp\left(\frac{i\omega l_b}{1 - M_d}\right) \end{aligned}$$

Balancing mass and momentum across the control volume and substituting ψ^+ and ψ^- , composite variables see equations (2.13a-b) in [8], into mass and momentum equations gives the following two coupled liner differential equations governing the behavior \hat{B} and \hat{u} [8].

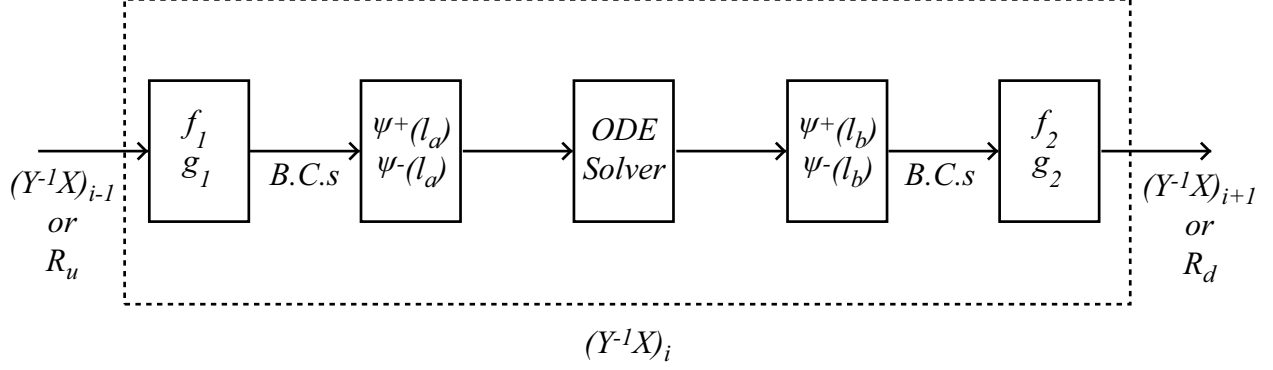


Figure 8: Module representation of the transfer matrix for a perforated liner.

$$\frac{d\psi^+}{dx} = -\frac{i\omega l}{1+\bar{u}}\psi^+ + \frac{1}{2}\frac{C_1 l}{S_p}\hat{v}_1 \quad (28)$$

$$\frac{d\psi^-}{dx} = \frac{i\omega l}{1+\bar{u}}\psi^- - \frac{1}{2}\frac{C_1 l}{S_p}\hat{v}_1 \quad (29)$$

Substitution of ψ^+ and ψ^- in equations (24)-(27) give the following boundary conditions

$$\begin{aligned} \psi^+(l_a) &= f_1 e_1, \quad \psi^+(l_b) = f_2 e_3 \\ \psi^-(l_a) &= g_1 e_2, \quad \psi^-(l_b) = g_2 e_4 \end{aligned}$$

The difference in stagnation enthalpy fluctuations across the liner can be related to \hat{v}_1 by employing the relationship for the liner compliance given by equation (2.1) in [8]. Using this compliance with the momentum equation in the normal direction and the relation $\hat{B} = \psi^+ + \psi^-$ gives [8]

$$\hat{v}_1(x) = \frac{\eta_1}{i\omega}[\hat{B}_1(x) - \psi^+(x) + \psi^-(x)]$$

where \hat{B}_1 represents fluctuation in stagnation enthalpy outside of the first liner. \hat{B}_1 is governed by the configuration of the perforated liner. The current liner model consists of a second in an annular cavity enclosing the first liner. The annular cavity is of the same length as the perforated liner with rigid wall at the ends. The second liner is assigned η_2 and C_2 as the compliance and the circumference respectively. A mass and momentum balance inside the cavity gives

$$\frac{d\hat{B}_1}{dx} = -i\omega\hat{u}_1 \quad (30)$$

$$\frac{d\hat{u}_1}{dx} = -i\omega\hat{B}_1 - \frac{C_1 l}{S_c}\hat{v}_1 + \frac{C_2 l}{S_c}\hat{v}_2 \quad (31)$$

$$\hat{v}_2(x) = \frac{\eta_2}{i\omega}[\hat{B}_2 - \hat{B}_1]$$

$$\hat{u}_1(l_a) = 0, \quad \hat{u}_1(l_b) = 0 \quad (32)$$

Note that S_c is the annular cross-sectional area between the first and the second liner. \hat{u}_1 is the fluctuating velocity in between the two liners. Also, $\hat{B}_2 \rightarrow 0$ for an annular cavity that is open to a reservoir of fluid flowing through the liners. Furthermore, the annular cavity ends are rigid walls.

The total compliance of the each liner is developed in [8] and is given by

$$\frac{1}{\eta} = \frac{\pi a^2}{\sigma l} \frac{1}{K_a} + \frac{t}{\sigma l} \quad (33)$$

where $\sigma = \pi a^2/d^2$ is the open-area ratio of the perforated screen. a , t and d is the orifice radius, the thickness of the liner and the distance between orifices respectively. K_a is the Rayleigh Conductivity and for low frequencies is given by equation (23). Equations (28),(29),(30) and (31) then form a closed set of four coupled liner differential equation governing the perforated liner system. This set of equations can easily be solved employing any robust numerical integration recipes available. To acquire frequency modes for a perforated liner it is vital to develop a technique which incorporates the solution for this set of equations in our current modular simulation tool. The technique is depicted in figure 8 below Where $(Y^{-1}X)_{i-1}$ is the transfer matrix from a previous element which gives the upstream wave amplitudes f_1 and g_1 for the liner. These amplitudes can be use with the upstream liner boundary, ψ^+ and ψ^- at $x = l_a$, to solve the set of equations governing the perforated liner, equations (28),(29),(30) and (31). Note that equations (30) and (31) use equations (32) as boundary conditions. The boundary condition at the end of the liner, ψ^+ and ψ^- at $x = l_b$, give the wave amplitudes downstream of the liner, f_2 and g_2 , or $(Y^{-1}X)_i$ the transfer matrix for the perforated liner. This transfer matrix can then be incorporated in our frequency mode solver to solve for modes of a system integrating a perforated liner.

4 Results

4.1 Effects of Time Delay on the Heuristic Flame Model

The ducted flame model consists of a choked inlet at the upstream end, $\dot{m}_o(x = 0) = 0$, and an open end at the downstream end, $p'(x = l) = 0$. The gas inside a LPP system is mostly air, so for simplicity the thermodynamic properties of air are used and assumed to be constant across the flame, i.e. the gas constant $R = 287 \text{ kJ/Kg/K}$ and the ratio of specific heats $\gamma = 1.4$. The mean Mach no. upstream of the flame $\bar{M}_1 = 0.05$ with a mean stagnation temperature $\bar{T}_{0,1} = 288 \text{ K}$. The jump in the mean stagnation temperature is taken to be $\bar{T}_{0,2}/\bar{T}_{0,1} = 6$. The flame is located at the center of the duct $b/l = 0.5$ and the fuel injector is located at $l_{inj}/l = 0.15$, therefore, the convective distance for the fuel to the flame is given by $(b - l_{inj})/l$. This convective distance is incorporated in τ_d , a convective time delay, to enforce the Rayleigh criterion hence instability. Note, all results in this and the subsequent sections are numerical and are a basis for future numerical and experimental studies.

Figure 9 (left) shows that the imaginary frequency solutions of the system (adapted flame model) are greater than zero. Since the harmonic pressure perturbation is given by $p'(x, t) = \hat{p} \exp(i\omega t)$ a positive imaginary solution results into a stable system. That is, the pressure perturbation decay

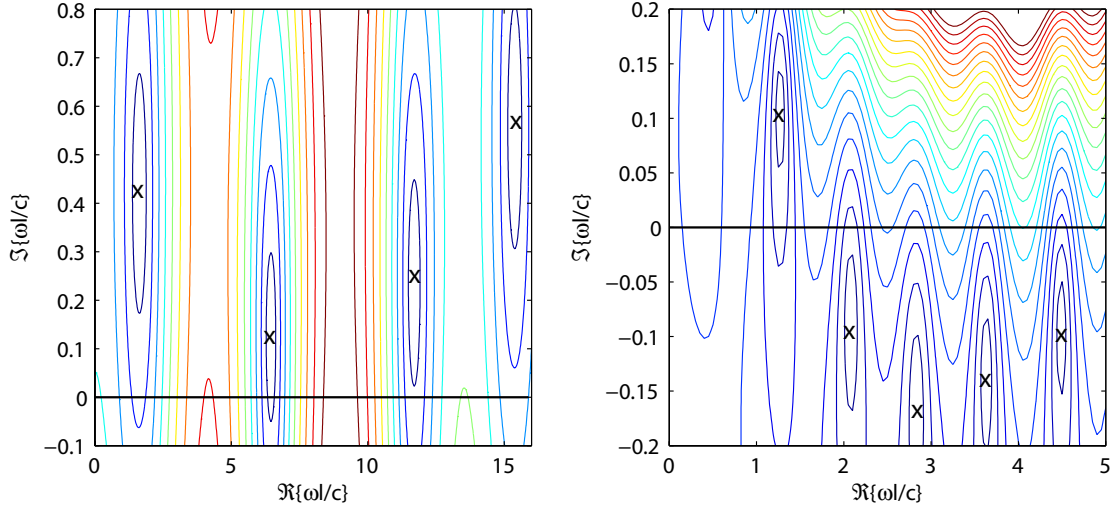


Figure 9: The simulation solves for the absolute value of the non-dimensional frequency hence the minimums are zeros, these minimums are denoted by "x" on the plots. Left is the flame model with out any time delay incorporation while right is the flame model with time delay mechanics.

with time. These numerical results agree with the physical aspects of the system as discussed in § 3.1.3.

Likewise figure 9 (right) shows that the inclusion of time delays shifts the imaginary frequency solutions of the system below zero resulting in an unstable system, where the pressure oscillations grow with time. These numerical results also agree with the theory employed to modify the system as discussed in § 3.1.3.

4.2 Ducted Helmholtz Resonator

The ducted Helmholtz resonator consists of an open end at both the upstream and the downstream end, $p' = 0$ at $x = 0$ and at $x = l$. Inside the duct standard pressure and temperature condition is assumed so the speed of sound $c = 340.29 \text{ m/s}$. The mean Mach no. upstream of the resonator $\bar{M}_1 = 0.05$ and the mean Mach no. in the neck of the resonator $\bar{M}_n = 0.02$. The mean Mach no. downstream of the resonator is approximately the same as the mean Mach no. upstream since the cross-sectional area ratio of the resonator neck opening and the duct is very small, $S_n/S_D = 0.002$. The resonator neck length, volume and location is taken to be $l_n/l = 0.005$, $V/lS_D = 0.002$ and $l_r/l = 0.5$.

Figure 10 displays frequency solutions of an open-end duct/ resonator system with a mean flow. One obvious point depicted by figure 10 is the importance of the placement of the resonator. The damping provided by the resonator is driven by the pressure oscillations the opening of the resonator experiences. That is, the higher the pressure oscillations at the opening the greater the damping. Figure 10 clearly agrees with this assessment such that at the first mode (an anti-node in an open-end duct) the resonator provides significant amounts of damping while at the second mode

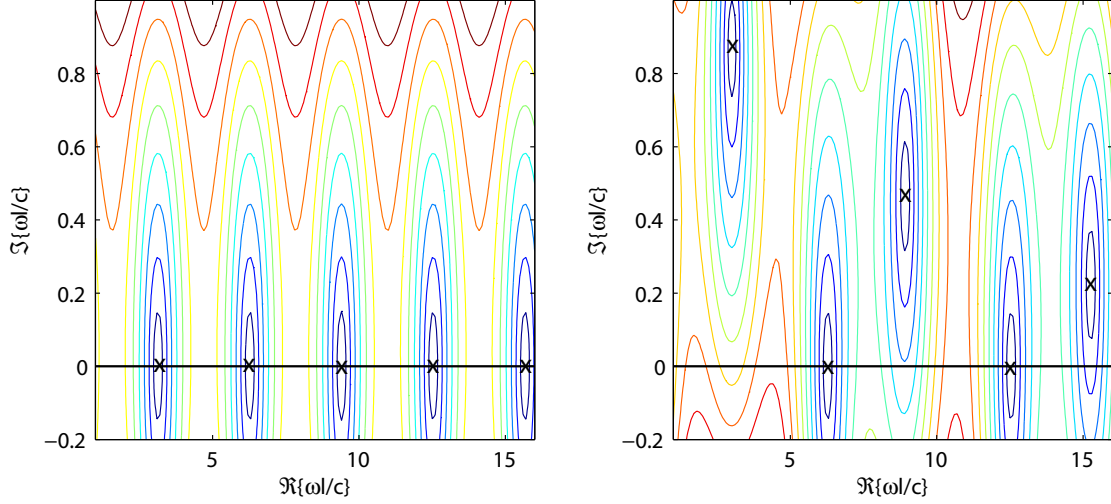


Figure 10: The simulation solves for the absolute value of the non-dimensional frequency hence the minimums are zeros, these minimums are denoted by "x" on the plots. Left is the simple open duct solution without a resonator while right is the resonator ducted system.

(a node at the resonator location in an open-end duct) the resonator provides no damping at all.

Moreover, figure 10 gives insight on how the resonance of the resonator impacts the system. Due to the location of the resonator, $l_r/l = 0.5$, the anti-nodes and node alternate, that is, all the odd modes are anti-nodes while all the even modes are nodes. The first and the third modes are both anti-nodes yet the damping provided by the first is greater than the third. Same is true for the third and fifth modes and so forth. Physically, a resonator is most effective at it's resonance due to the large amplitude of oscillations experienced by the system. Whether the first mode is closer to the resonance over the third mode and so forth can be seen by examining the impedance provided by the resonator at these modes, please see figure 12. The impedance is closest to resonance at mode 1 and diverges with mode increment, satisfying yet another physical aspect of a Helmholtz resonator.

4.3 Perforated Liner with Bias Flow

The ducted perforated liner with bias flow system consists of an open end at both the upstream and the downstream end, $p' = 0$ at $x = 0$ and at $x = l$. Inside the duct standard pressure and temperature condition is assumed so the speed of sound $c = 340.29 \text{ m/s}$. The mean Mach no. upstream of the liner $\bar{M}_1 = 0.046$ and the mean flow through the liner is taken to be $\bar{M}_{l,1} = 0.03$. The liner's center is located at the center of the duct and the liner is of length $l_p/l = 0.19$. The diameter of the duct is 12.7 cm and the length of the liner $l_p = 17.8 \text{ cm}$. The liner is perforated by a regular lattice of holes of diameter 0.75 mm and spacing 3.3 mm , which is equivalent to an open-area ration of the perforated screen for liner 1 $\sigma_1 = 0.040$. The first liner is enclosed in a second liner of equal length and of diameter 15.2 cm . The second liner is perforated by holes of diameter 2.7 mm and spacing 17.0 mm corresponding to $\sigma_2 = 0.020$. The thickness of both liners

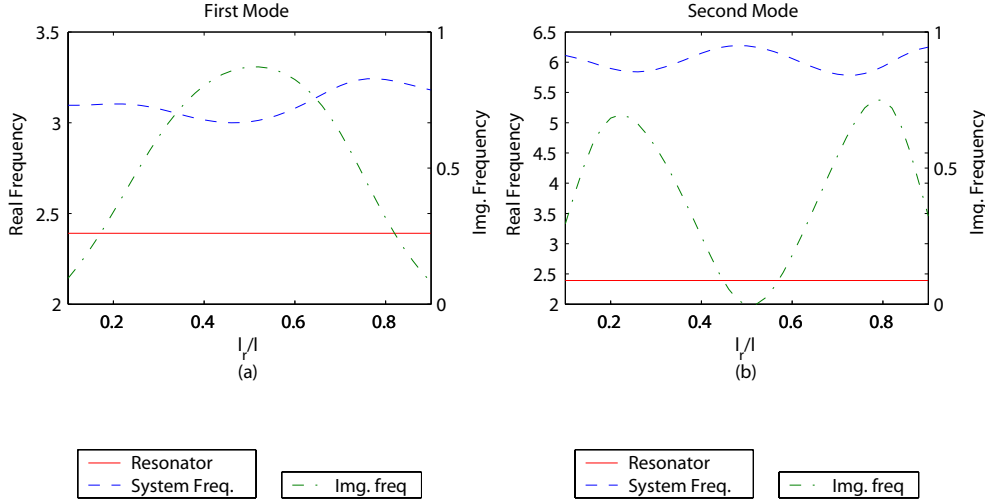


Figure 11: Effect of varying the location of the resonator on the system frequency, and the imaginary frequency at two different modes. The resonator frequency is shown for reference.

is 3 *mm*.

Note, the perforated liner as a damper has similarities and differences with the Helmholtz resonator, see § 4.2. One obvious difference is that the liner shifts the real frequencies. This shift can be monitored by plotting the root locus of one of the modes, see figure 14. Another difference is that the second and the fourth mode, which are both anti-nodes, exhibit some damping while in the case of the resonator they exhibited none. To elaborate, unlike the liner the resonator is a point-wise damper so when it is located over a pressure node, the resonator as a damper becomes ineffective. While, though the liner does experience a pressure node due to the physical dimension of the liner the average pressure perturbation is not zero within the liner. The similarity here is that both dampers rely on pressure fluctuation to dissipate acoustic energy, which makes sense since both dampers use Rayleigh conductivity as a dissipative mechanism.

5 Conclusion

Lean premixed prevaporized (LPP) gas turbine generators are popular in energy generation applications to meet strict emission requirements. Because the combustion process is very lean, combustion instabilities due to acoustic perturbations are more likely to occur than in a less lean fuel combustion process. In this work, a modular simulation tool is developed to examine the interaction of plane acoustic waves with typical combustion system elements. The simulation tool focuses on representing these interactions in the form of transfer matrices. These transfer matrices then acts as modules, which can be placed in any desired configuration with ease. A heuristic gain-delay flame model is represented in a transfer matrix, which can be used to test damping devices. Similarly, transfer matrices representing a Helmholtz resonator and a perforated liner with bias flow are developed, based on models that have been experimentally validated in previous work. These dampers will facilitate the stabilization of thermoacoustic instabilities generated by the heuristic

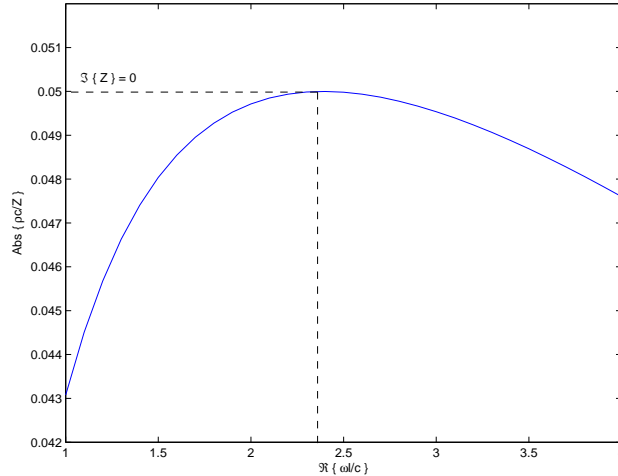


Figure 12: The non-dimensional admittance of the resonator for varying resonator frequencies

flame model.

In ongoing work, optimization for each specific system will be explored by evaluating the effect of Helmholtz and liner parameters on the suppression of instabilities in the model. The results obtained in this work will be used to design future laboratory-scale experiments, for the purposes of validation as well as for developing new strategies for damping of combustion dynamics in commercial gas turbines.

References

- [1] V. Bellucci, P. Flohr, C. O. Paschereit, and F. Magni. On the use of helmholtz resonators for damping acoustic pulsations in industrial gas turbines. *ASME J. Eng. Gas Turb. Pow.*, 126(2):271–275, December 2000.
- [2] S. Candel, D. Durox, and T. Schuller. Flame interactions as a source of noise and combustion instabilities. *AIAA/CEAS 10th Aeroacoustics Conf. Manchester, UK*, 2004.
- [3] S. M. Correa. Power generation and aeropropulsion gas turbines: from combustion science to combustion tech. *Proc. 27th Int. Symp. Combust.*, 2:1793–1807, 1998.
- [4] L. Crocco and S. I. Cheng. Theory of combustion instability in liquid propellant rocket motors. *London: Butterworths*, 1956.
- [5] Ivor J. Day, Ann P. Dowling, Ian D.J. Dupère, and Claire Peyrache. Acoustic absorbers for lpp combustors. Cambridge University Engineering Department.
- [6] A. P. Dowling. The calculation of thermoacoustic oscillations. *J. Sound Vib.*, 180(4):557–581, November 1995.
- [7] A. P. Dowling and J. E. Ffowcs Williams. *Sound and Sources of Sound*. John Wiley and Sons, New York, NY, 1983.

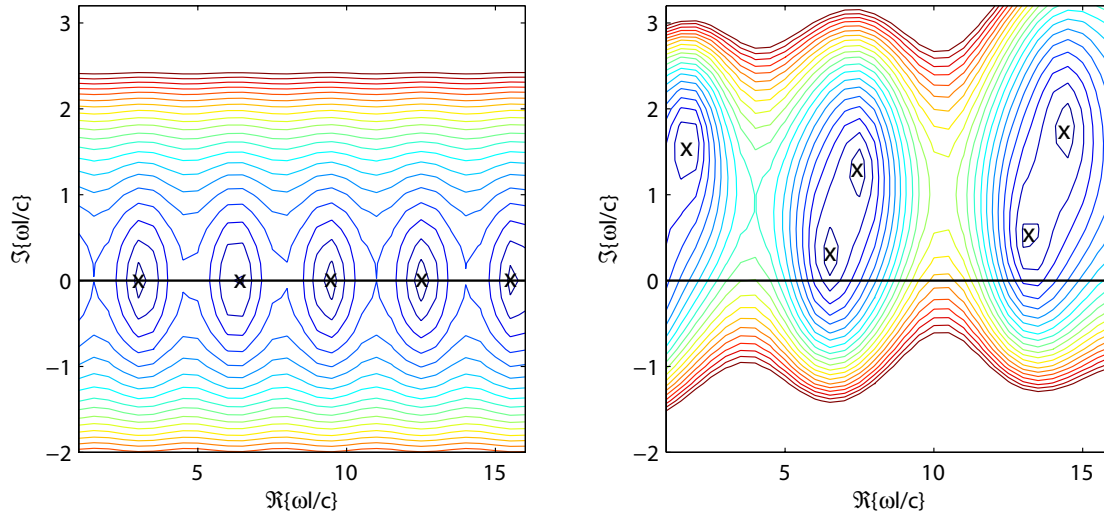


Figure 13: The simulation solves for the absolute value of the non-dimensional frequency hence the minimums are zeros, these minimums are denoted by "x" on the plots. Left is a simple duct with no liner and right is the effect of the liner on the frequencies.

- [8] J. D. Eldredge and A. P. Dowling. The absorption of axial acoustic waves by a perforated liner with bias flow. *J. Fluid Mech.*, 485:307–335, January 2003.
- [9] F. Guliani, P. Gajan, O. Dires, and M. Ledoux. Influence of pulsed entries on a spray generated by an airblast injection device: an experimental analysis on combustion instability processes in aeroengines. *Proc. Combust. Inst.*, 29:91–98, 2003.
- [10] P. Hill and C. Peterson. *Mechanics and Thermodynamics of Propulsion*. Prentice Hall, New York, NY, 1991.
- [11] M. S. Howe. On the theory of unsteady high Reynolds number flow through a circular aperture. *Proc. Roy. Soc. A*, 105:385–396, 1979.
- [12] T. Lieuwen, H. Torres, C. Johnson, and B. T. Zinn. A mechanism of combustion instability in lean premixed gas turbine combustors. *ASME J. Eng. Gas Turb. Pow.*, 123:182–188, January 2001.
- [13] H. C. Mongia, T. J. Held, G. C. Hsiao, and R. P. Pandalai. Challenges and progress in controlling dynamics in gas turbine combustors. *J. Prop. Power*, 19(5):822–829, 2003.
- [14] G. A. Richard and M. C. Janus. Characterization of oscillations during preix gas turbine combustion. *ASME J. Eng. Gas Turb. Pow.*, 120:294–302, 1998.
- [15] K. Schadow and V. Yang. Active combustion control for propulsion systems. *AGARD workshop Rep.*, 1996.
- [16] M. Zhu, A. P. Dowling, and K. N. C. Bray. Self-escited oscillations in combustors with spray atomizers. *ASME J. Eng. Gas Turb. Pow.*, 123(4):779–786, 2001.

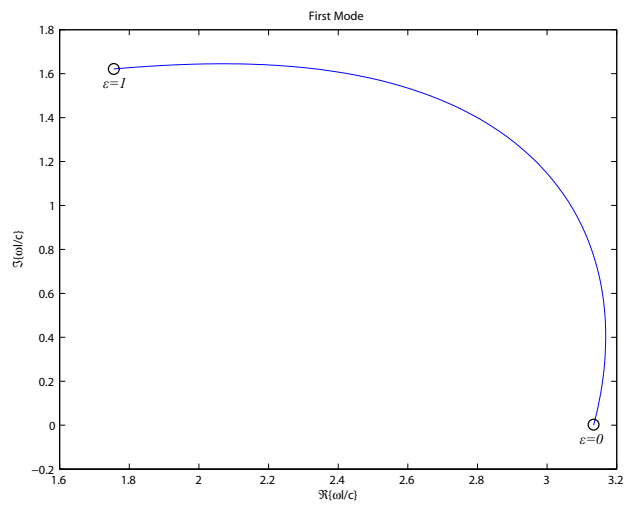


Figure 14: Root locus of the first mode. This plot is generated by modifying the effective compliance for the first liner as $\eta_{eff,1} = \epsilon\eta_1$. So, $\epsilon = 0$ corresponds no compliance or the first liner acts as rigid wall reducing the system to a simple duct problem. $\epsilon = 1$ corresponds to the compliance of the first liner.